

Multi-target ranging using an optical reservoir computing approach in the laterally coupled semiconductor lasers with self-feedback

Dong-Zhou Zhong(钟东洲), Zhe Xu(徐喆), Ya-Lan Hu(胡亚兰), Ke-Ke Zhao(赵可可), Jin-Bo Zhang(张金波),Peng Hou(侯鹏), Wan-An Deng(邓万安), and Jiang-Tao Xi(习江涛)

Citation: Chin. Phys. B, 2022, 31 (**7**): 074205. DOI: 10.1088/1674-1056/ac4021

Journal homepage: http://cpb.iphy.ac.cn; http://iopscience.iop.org/cpb

What follows is a list of articles you may be interested in

Enhancing performance of GaN-based LDs by using GaN/InGaN asymmetric lower waveguide layers

Wen-Jie Wang(王文杰), Ming-Le Liao(廖明乐), Jun Yuan(袁浚), Si-Yuan Luo(罗思源), and Feng Huang(黄锋)

Chin. Phys. B, 2022, 31 (**7**): 074206. DOI: 10.1088/1674-1056/ac597c

Improved thermal property of strained InGaAlAs/AlGaAs quantum wells for 808-nm vertical cavity surface emitting lasers

Zhuang-Zhuang Zhao(赵壮壮), Meng Xun(荀孟), Guan-Zhong Pan(潘冠中), Yun Sun(孙昀), Jing-Tao Zhou(周静涛), and De-Xin Wu(吴德馨)

Chin. Phys. B, 2022, 31 (**3**): 034208. DOI: 10.1088/1674-1056/ac16d0

GaSb-based type-I quantum well cascade diode lasers emitting at nearly 2-μm wavelength with digitally grown AlGaAsSb gradient layers

Yi Zhang(张一), Cheng-Ao Yang(杨成奥), Jin-Ming Shang(尚金铭), Yi-Hang Chen(陈益航), Tian-Fang Wang(王天放), Yu Zhang(张宇), Ying-Qiang Xu(徐应强), Bing Liu(刘冰), and Zhi-Chuan Niu(牛智川)

Chin. Phys. B, 2021, 30 (**9**): 094204. DOI: 10.1088/1674-1056/abe930

An approach to gas sensors based on tunable diode laser incomplete saturated absorption spectra

Wei Nie(聂伟), Zhen-Yu Xu(许振宇), Rui-Feng Kan(阚瑞峰), Mei-Rong Dong(董美蓉), and Ji-Dong Lu(陆继东)

Chin. Phys. B, 2021, 30 (**6**): 064213. DOI: 10.1088/1674-1056/abd769

Random-injection-based two-channel chaos with enhanced bandwidth and suppressed time-delay signature by mutually coupled lasers: Proposal and numerical analysis

Shi-Rong Xu(许世蓉), Xin-Hong Jia (贾新鸿), Hui-Liang Ma(马辉亮), Jia-Bing Lin(林佳兵), Wen-Yan Liang(梁文燕), and Yu-Lian Yang(杨玉莲)

Chin. Phys. B, 2021, 30 (**1**): 014203. DOI: 10.1088/1674-1056/abb228

Multi-target ranging using an optical reservoir computing approach in the laterally coupled semiconductor lasers with self-feedback

Dong-Zhou Zhong(钟东洲)[1,†], Zhe Xu(徐喆)[1], Ya-Lan Hu(胡亚兰)[1], Ke-Ke Zhao(赵可可)[1], Jin-Bo Zhang(张金波)[1], Peng Hou(侯鹏)[1], Wan-An Deng(邓万安)[1], and Jiang-Tao Xi(习江涛)[1,2]

[1] *Intelligent Manufacturing Faculty, Wuyi University, Jiangmen* 529020, *China*

[2] *School of Electrical, Computer, Telecommunications Engineering, University of WollongGong*, 2522, *Australia*

(Received 8 October 2021; revised manuscript received 30 November 2021; accepted manuscript online 5 December 2021)

We utilize three parallel reservoir computers using semiconductor lasers with optical feedback and light injection to model radar probe signals with delays. Three radar probe signals are generated by driving lasers constructed by a three-element laser array with self-feedback. The response lasers are implemented also by a three-element lase array with both delay-time feedback and optical injection, which are utilized as nonlinear nodes to realize the reservoirs. We show that each delayed radar probe signal can be predicted well and to synchronize with its corresponding trained reservoir, even when parameter mismatches exist between the response laser array and the driving laser array. Based on this, the three synchronous probe signals are utilized for ranging to three targets, respectively, using Hilbert transform. It is demonstrated that the relative errors for ranging can be very small and less than 0.6%. Our findings show that optical reservoir computing provides an effective way for applications of target ranging.

Keywords: coupled semiconductor lasers, lidar ranging, optical reservoir computing, chaos synchronization

PACS: 42.55.Px, 42.65.Sf, 42.79.Ta, 42.60.Mi **DOI:** 10.1088/1674-1056/ac4021

1. Introduction

The chaotic lidar is a lidar system utilizing the nonlinear dynamics of semiconductor lasers.[1–3] A chaotic lidar can be used as an enabling technology for many applications, such as artificial intelligence, precision range finding, object tracking and locating, through-wall detection, driverless navigation system and so on.[4–7,13–19] Among other applications, chaotic lidar ranging (CLR) has attracted considerable attention due to its advantages over short-pulse and continuous wave (CW) lidar ranging, such as low probability of intercept, high resolution in ranging and velocity, strong anti-interference ability, easy generation and low cost.[1–3,8]

There are mainly two ways for the implementation of CLRs. The first one is based on the computation of the cross-correlation between the reflected return signal and the replica of the signal transmitted.[1–9,15,16] Such correlation-based methods take advantage of the broad bandwidth of the chaotic laser and can achieve resolution up to centimeter-level. Although progress was made to increase the resolution[4–9] in recent years, further improvement becomes very difficult due to the limit of the correlation and the interference of spontaneous emission noise and channel noise. Another way of implementing CRLs is with a synchronized chaotic lidar. A synchronization chaotic lidar system has two chaotic lasers: one called the drive laser, used to generate the probe signal, and the other referred to as response laser that is used to synchronize with the drive laser. In order to probe the target, the drive laser output is modulated with a microwave signal. The chaotic probe signal with a microwave signal is reflected by the target, then delayed, finally synchronized with a chaotic signal from the response laser output. The delayed microwave signal is decoded by using high-quality chaotic synchronization. The delay time in the microwave is extracted by using Hilbert transform. The distance of the target at an arbitrary position can be calculated by using delay time. In contrast to a cross-correlation-based chaotic lidar, synchronized chaotic lidars has the potential to provide improved ranging performance in accuracy and anti-noise ability since the quality of synchronization is very robust to noise.[18–20]

The accuracy of the target ranging associated with synchronized chaotic lidar systems heavily depends on the quality and stability of chaotic synchronization. However, all existing techniques for completing chaos synchronization rely on the assumptions that the drive and the response laser systems are identical, i.e., the rate-equations describing the two lasers must be the same and known a priori.[21–23] However, these assumptions do not hold in practice, as an inevitable mismatch always exists between the driving and response lasers.

In recent years, reservoir computing (RC) has been proven to be an effective approach in the prediction of chaotic systems from data.[24–27] The delay-based RC first proposed by Appeltant *et al.*,[28] composed of a nonlinear node and a delay feedback loop, is proved to be an effective and simple hardware implementation for neural network computing in hardware.[29–38] Many hardware implementations of such delay-based RC have been reported in literature, such

[†]Corresponding author. E-mail: dream_yu2002@126.com

© 2022 Chinese Physical Society and IOP Publishing Ltd

as the electronic system,[29,30] opto-electronic system,[31,32] all-optical system,[33–35] and laser dynamical system.[36–38] Among these techniques, the delay-based RC using nonlinear semiconductor lasers has the advantages of fast-speed, high efficiency and parallel computing capability for many benchmark tasks,[33–48] such as time series prediction,[39–43] optical packet header recognition,[44] speech recognition,[45] nonlinear channel equalization[46] and so on. A growing number of studies have shown that a well-trained reservoir computer can be well synchronized with its learned chaotic system by using a delay-based RC approach.[24–27] For example, in 2017, Anonik *et al.* proved experimentally that a reservoir can be trained to yield similar dynamics to its learned chaotic system (similar spectrum, Lyapunov index, etc).[47] Our previous work further shows that high-quality chaotic synchronization between the driving laser array and its trained reservoir in the existence of mismatch between their rate equations can be achieved by using a delay-based optical reservoir computing approach.[42]

The 1-D lateral laser array (laterally coupled semiconductor lasers) with rich chaos dynamics represents an ideal candidate of an integrated chaotic light source, which has potential applications in multi-target chaotic lidar synchronous ranging. Compared with the multi-target ranging based on three uncoupled semiconductor lasers, the ranging to multi-target based on the 1-D lateral laser array are advantageous by a simple structure and thus there is easy fabrication on a single chip. For the application for the multi-target ranging using the 1-D lateral laser array, it is necessary to overcome the limitations of traditional optical chaos synchronization theory as described above.[21–23] The delay-based RC technology in training optical chaos synchronization provides a possible solution for this problem.[42] The stable and high-accuracy ranging to the multi-target can be achieved in the delay-based optical reservoir computing system based on the 1-D lateral laser array, owing to the realization of stable and high-quality chaos synchronization by the predictive learning, even if the existences of parameter mismatches between the driving laser element and its trained reservoir.

Motivated by these described above, in this paper, as shown in Fig. 1, we propose three parallel delay-based optical chaotic RCs using laterally coupled semiconductor lasers both subject to self-feedback and optical injection, where the light injected into each laser is modulated by a delayed reflection probe signal from a target. These RCs can be described by the coupled wave theory developed by our previous work.[48] Based on these three-parallel delay-based RCs and Hilbert phase transformation principle, we further propose a novel scheme for multi-channel synchronized chaotic lidar ranging for multiple targets. For this scheme, we demonstrate the quality and stability of the lag chaos synchronization between a well-trained reservoir computer and its learned delay probe signal with a microwave signal. We explore the influences of the delay-time of RC and the interval of the virtual nodes on the training errors. Finally, we discuss the accuracies and the relative errors of the multi-target ranging.

2. Experimental setup and theoretical method

2.1. Experimental setup

Figure 1 depicts a schematic diagram of synchronized chaotic lidar ranging for multi-targets by using three parallel delay-based RCs. Here, TLC-SL represents three laterally coupled semiconductor lasers, also referred to as a three-element laser array. The TLC-SL_1 and TLC-SL_2 are the driving and response laser arrays, respectively. They both have three identical laser waveguides (LWGs) of width $2a$, which are edge-to-edge separated $2d$. The LWG A locates between the LWG B and the LWG C. The LWGs A, B, and C in the TLC-SL_1 are also denoted as lasers A_1, B_1 and C_1, respectively, and those in the TLC-SL_2 are also called as lasers A_2, B_2, and C_2, respectively. The three driving laser elements in the TLC-SL_1 are chaotic radar sources to be learned for their synchronizations. With both delay-time feedback and optical injection, the three response laser elements in the TLC-SL_2 are utilized as nonlinear nodes to realize three-parallel delay RCs. The six neutral density filters (NDFs) are used to control light strength. The variable attenuators (VAs) are used to control the feedback strengths. The optical isolators (ISs) are applied to avoid light feedback. The AM_1, AM_2, and AM_3 are amplitude modulators. m_A, m_B and m_C are the sinusoidal microwave signals. The fiber beam splitters (FBSs) ($s = 1$–3) separate the output light into the photodetector and the input layer, respectively. The FBS_4 divides the external light from the driving semiconductor laser (D-SL) into three identical components, which are respectively injected into three phase modulations (PM_1, PM_2 and PM_3).

The system presented by Fig. 1 is composed of the transmitting module (TM), multi-target detection module (MTDM), three input layers, three parallel reservoirs, three output layers and ranging calculation modules (RCMs). In the TM and MTDM, three beams of chaotic light waves are respectively emitted by lasers A_1, B_1 and C_1 with self-feedback, and they are respectively modulated with m_A, m_B, and m_C (sinusoidal microwave signals) using amplitude modulators, and these amplitude-modulated chaotic light waveforms are called the probe signals, such as PS-A, PS-B, and PS-C. These three probe signals are transmitted to by the optical transmitting antennas (OTA_{1-3}), then reflected by the three targets and back to the optical receiving antennas (ORAs). Note that the signals collected by the receiving antennas can be considered as a delayed version of the three probe signals, which are denoted as $u_A(t-\tau_A)$, $u_B(t-\tau_B)$ and $u_C(t-\tau_C)$.

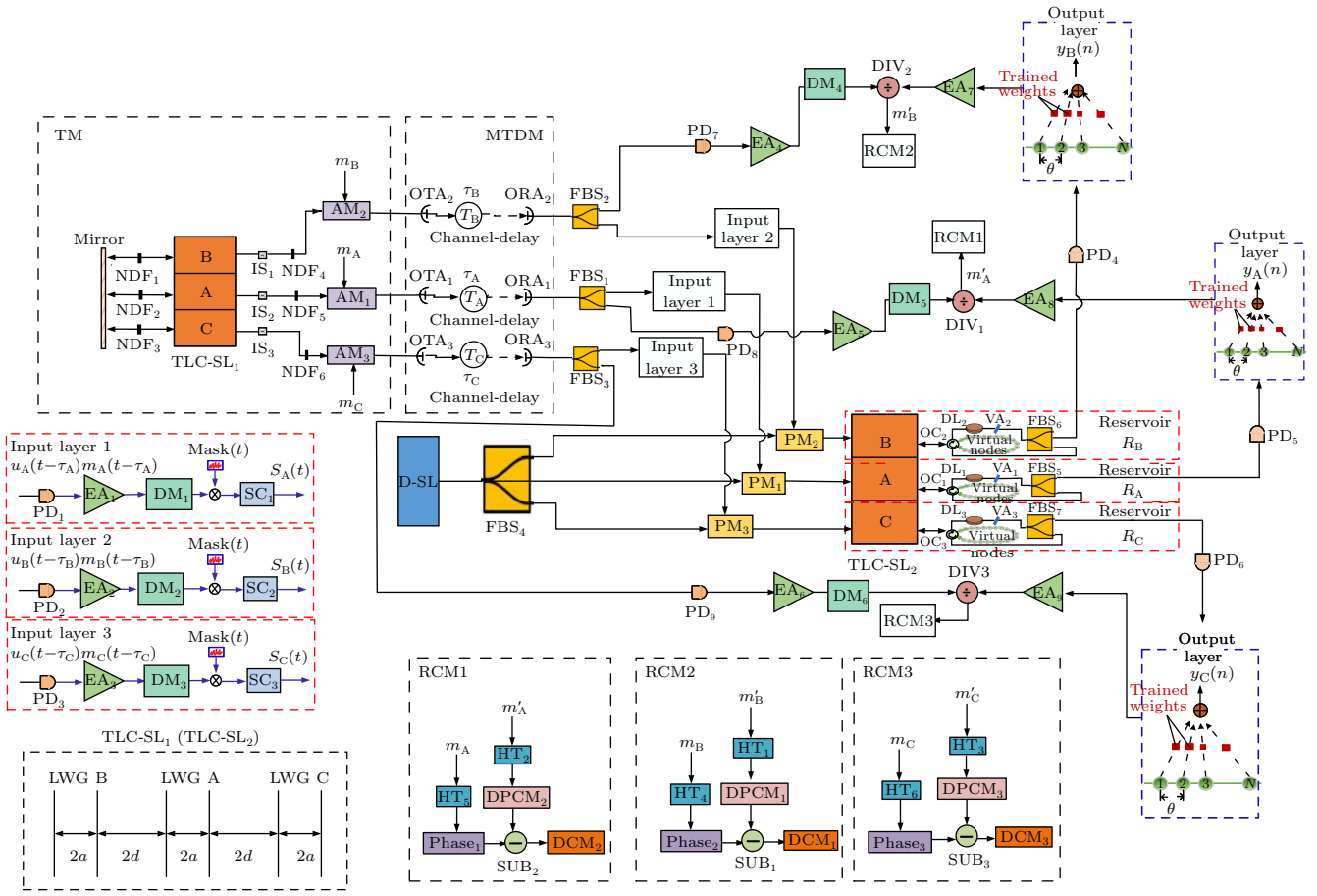


Fig. 1. Schematic diagram of synchronized chaotic lidar ranging for the multi-target by utilizing three parallel delay-based optical reservoir computers using three laterally coupled semiconductor lasers (see texts for the detailed description).

The input layers provide input connections to the reservoirs. Here, signals collected from the ORAs are first converted into current signal by photoelectric detections (PDs), and then amplified by the electric amplifiers (EA_{1-3}), and then sampled as input data by the discrete modules (DM_{1-3}), which are denoted as u_A (n'_A), u_B (n'_B), and u_C (n'_C), respectively. Here, $n'_A = n - k_A$, $n'_B = n - k_B$, and $n'_C = n - k_C$. n is the discrete time index, k_A, k_B, and k_C are the discrete length of channel-delays τ_A, τ_B, and τ_C. These sampled data holding for T and they are multiplied by a mask signal (named as Mask) with the periodicity T. These three Masks are chaotic signals generated by two mutually-coupled SLs, which are presented in Ref. [49]. These mask signals are scaled by a scaling factor γ using the scaling operation circuit (SC), yielding the out signals of the input layer, denoted as $S_A(t)$, $S_B(t)$, and $S_C(t)$, respectively. Then by means of phase modulators (PM_1, PM_2, and PM_3), they are modulated into the phase of the optical field of from the D-SL output, where the D-SL is a distributed feedback semiconductor laser. These phase-modulated light signals will be injected into responding laser fields in TLC-SL_2.

Within the reservoirs, the response lasers A_2, B_2, and C_2 in the TLC-SL_2 with both delay-time feedback and optical injection will exhibit chaotic dynamics, and hence they are utilized as nonlinear nodes to implement three parallel reservoirs, denoted as R_A, R_B, and R_C, respectively. The feedback time along any of the delay lines (DL_1, DL_2, and DL_3) is considered as τ_2 in the response lasers. The interval between two adjacent nodes is set as θ. The number N of the virtual nodes along each delay line satisfies $N = T/\theta$. We consider that $\tau_2 = T + \theta$, indicating the case of desynchronization because that the reservoir loop with respect to the input and output layers allows for the coupling of each internal variable to one of its neighbors.[33,50]

In the output layers, the states of N virtual nodes along these three delay lines are first converted into current signals by the PDs. These current signals that are weighted and linearly summed up are denoted as $y_A(n)$, $y_B(n)$, and $y_C(n)$, respectively. Here, the weights need to be trained using a linear least-squares method that minimizes the mean-square error between each input signal and its corresponding reservoir output.[36,50] In such a system, by training the output weights, $y_A(n)$, $y_B(n)$, and $y_C(n)$ can be well synchronized with the delayed probe signals u_A (n'_A), u_B (n'_B), and u_C (n'_C), respectively.

In the RCMs (ranging calculation modules), signal m_A is decoded from the synchronous division between $u_A(n'_A)$ and $y_A(n)$ by the divider 1 (DIV_1), yielding m'_A, with a delay with

respect to $m_{\rm A}$. $m_{\rm B}$ is decoded from that between $u_{\rm B}(n'_{\rm B})$ and $y_{\rm B}(n)$ by the DIV$_2$, yielding $m'_{\rm B}$ with a delay. $m_{\rm C}$ is decoded from $u_{\rm C}(n'_{\rm C})$ and $y_{\rm C}(n)$ by the DIV$_3$, yielding $m'_{\rm C}$ with a delay. The phases of $m_{\rm A}$, $m_{\rm B}$, and $m_{\rm C}$ are extracted by the Hilbert transform (HT). The delay phases of $m'_{\rm A}$, $m'_{\rm B}$, and $m'_{\rm C}$ are obtained by the HT and DPCM (delay phase calculation module). Then phase differences $\Delta\phi_{m_{\rm A}}$, $\Delta\phi_{m_{\rm B}}$, and $\Delta\phi_{m_{\rm C}}$ are calculated by the subtracters (SUBs), where $\Delta\phi_{m_{\rm A}}$ is the phase difference between $m_{\rm A}$ and $m'_{\rm A}$, $\Delta\phi_{m_{\rm B}}$ is that between $m_{\rm B}$ and $m'_{\rm B}$, $\Delta\phi_{m_{\rm C}}$ is that between $m_{\rm C}$ and $m'_{\rm C}$. According to the constraint relationship between the target distances and phase differences (see Eqs. (28)–(32)), the distances of these targets ($\rm T_A$, $\rm T_B$, and $\rm T_C$) can be calculated by using the DCMs (distance calculation modules).

2.2. Theoretical method

The nonlinear dynamics of the three laser-elements in the TCL-SL$_1$ with self-feedback can be described by the coupled mode theory developed by our previous work presented in Ref. [48] as follows:

$$\begin{aligned}\frac{{\rm d}Y_{\rm A}^{(1)}(t)}{{\rm d}t} &= \frac{1}{2\tau_{\rm p}^{(1)}}(M_{\rm A}^{(1)}(t)-1)Y_{\rm A}^{(1)}(t)\\ &-Y_{\rm B}^{(1)}(t)(\eta_{\rm r}^{(1)}\sin\phi_{\rm BA}^{(1)}(t)+\eta_{\rm i}^{(1)}\cos\phi_{\rm BA}^{(1)}(t))\\ &-Y_{\rm C}^{(1)}(t)(\eta_{\rm r}^{(1)}\sin\phi_{\rm CA}^{(1)}(t)+\eta_{\rm i}^{(1)}\cos\phi_{\rm CA}^{(1)}(t))\\ &+k_{\rm f1}Y_{\rm A}^{(1)}(t-\tau)\cos(\phi_{\rm A}^{(1)}(t)\\ &+\omega_1\tau-\phi_{\rm A}^{(1)}(t-\tau)),\end{aligned}\tag{1}$$

$$\begin{aligned}\frac{{\rm d}Y_{\rm B}^{(1)}(t)}{{\rm d}t} &= \frac{1}{2\tau_{\rm p}^{(1)}}(M_{\rm B}^{(1)}(t)-1)Y_{\rm B}^{(1)}(t)\\ &+Y_{\rm A}^{(1)}(t)(\eta_{\rm r}^{(1)}\sin\phi_{\rm BA}^{(1)}(t)-\eta_{\rm i}^{(1)}\cos\phi_{\rm BA}^{(1)}(t))\\ &-Y_{\rm C}^{(1)}(t)(\eta_{\rm r2}^{(1)}\sin\phi_{\rm CB}^{(1)}(t)+\eta_{\rm i2}^{(1)}\cos\phi_{\rm CB}^{(1)}(t))\\ &+k_{\rm f2}Y_{\rm B}^{(1)}(t-\tau)\cos(\phi_{\rm B}^{(1)}(t)\\ &+\omega_1\tau-\phi_{\rm B}^{(1)}(t-\tau)),\end{aligned}\tag{2}$$

$$\begin{aligned}\frac{{\rm d}Y_{\rm C}^{(1)}(t)}{{\rm d}t} &= \frac{1}{2\tau_{\rm p}^{(1)}}(M_{\rm C}^{(1)}(t)-1)Y_{\rm C}^{(1)}(t)\\ &+Y_{\rm A}^{(1)}(t)(\eta_{\rm r}^{(1)}\sin\phi_{\rm CA}^{(1)}(t)-\eta_{\rm i}^{(1)}\cos\phi_{\rm CA}^{(1)}(t))\\ &+Y_{\rm B}^{(1)}(t)(\eta_{\rm r2}^{(1)}\sin\phi_{\rm CB}^{(1)}(t)-\eta_{\rm i2}^{(1)}\cos\phi_{\rm CB}^{(1)}(t))\\ &+k_{\rm f3}Y_{\rm C}^{(1)}(t-\tau)\cos(\phi_{\rm C}^{(1)}(t)\\ &+\omega_1\tau-\phi_{\rm C}^{(1)}(t-\tau)),\end{aligned}\tag{3}$$

$$\frac{{\rm d}M_j^{(1)}(t)}{{\rm d}t} = \frac{1}{\tau_{\rm n}^{(1)}}[Q^{(1)}-M_j^{(1)}(t)(1+(Y_j^{(1)}(t))^2)],\tag{4}$$

$$\begin{aligned}\frac{{\rm d}\phi_{\rm A}^{(1)}(t)}{{\rm d}t} &= -\frac{\alpha_H^{(1)}}{2\tau_{\rm p}^{(1)}}(M_{\rm A}^{(1)}-1)+(\omega_1-\Omega_{\rm A})\\ &+\frac{Y_{\rm B}^{(1)}(t)}{Y_{\rm A}^{(1)}(t)}(\eta_{\rm r}^{(1)}\cos\phi_{\rm BA}^{(1)}(t)-\eta_{\rm i}^{(1)}\sin\phi_{\rm BA}^{(1)}(t))\\ &+\frac{Y_{\rm C}^{(1)}(t)}{Y_{\rm A}^{(1)}(t)}(\eta_{\rm r}^{(1)}\cos\phi_{\rm CA}^{(1)}(t)-\eta_{\rm i}^{(1)}\sin\phi_{\rm CA}^{(1)}(t))\\ &-k_{\rm f1}\frac{Y_{\rm A}^{(1)}(t-\tau)}{Y_{\rm A}^{(1)}(t)}\sin(\phi_{\rm A}^{(1)}(t)\\ &+\omega_1\tau-\phi_{\rm A}^{(1)}(t-\tau)),\end{aligned}\tag{5}$$

$$\begin{aligned}\frac{{\rm d}\phi_{\rm B}^{(1)}(t)}{{\rm d}t} &= -\frac{\alpha_H^{(1)}}{2\tau_{\rm p}^{(1)}}(M_{\rm B}^{(1)}-1)+(\omega_1-\Omega_{\rm B})\\ &+\frac{Y_{\rm A}^{(1)}(t)}{Y_{\rm B}^{(1)}(t)}(\eta_{\rm r}^{(1)}\cos\phi_{\rm BA}^{(1)}(t)+\eta_{\rm i}^{(1)}\sin\phi_{\rm BA}^{(1)}(t))\\ &+\frac{Y_{\rm C}^{(1)}(t)}{Y_{\rm B}^{(1)}(t)}(\eta_{\rm r2}^{(1)}\cos\phi_{\rm CB}^{(1)}(t)-\eta_{\rm i2}^{(1)}\sin\phi_{\rm CB}^{(1)}(t))\\ &-k_{\rm f2}\frac{Y_{\rm B}^{(1)}(t-\tau)}{Y_{\rm B}^{(1)}(t)}\sin(\phi_{\rm B}^{(1)}(t)\\ &+\omega_1\tau-\phi_{\rm B}^{(1)}(t-\tau)),\end{aligned}\tag{6}$$

$$\begin{aligned}\frac{{\rm d}\phi_{\rm C}^{(1)}(t)}{{\rm d}t} &= -\frac{\alpha_H^{(1)}}{2\tau_{\rm p}^{(1)}}(M_{\rm C}^{(1)}-1)+(\omega_1-\Omega_{\rm C})\\ &+\frac{Y_{\rm A}^{(1)}(t)}{Y_{\rm C}^{(1)}(t)}(\eta_{\rm r}^{(1)}\cos\phi_{\rm CA}^{(1)}(t)+\eta_{\rm i}^{(1)}\sin\phi_{\rm CA}^{(1)}(t))\\ &+\frac{Y_{\rm B}^{(1)}(t)}{Y_{\rm C}^{(1)}(t)}(\eta_{\rm r2}^{(1)}\cos\phi_{\rm CB}^{(1)}(t)+\eta_{\rm i2}^{(1)}\sin\phi_{\rm CB}^{(1)}(t))\\ &-k_{\rm f3}\frac{Y_{\rm C}^{(1)}(t-\tau)}{Y_{\rm C}^{(1)}(t)}\sin(\phi_{\rm C}^{(1)}(t)\\ &+\omega_1\tau-\phi_{\rm C}^{(1)}(t-\tau)).\end{aligned}\tag{7}$$

In the reservoir layers, the dynamics of the three laser-elements in the TCL-SL$_2$ with both delay-time feedback and optical injection can be modeled as

$$\begin{aligned}\frac{{\rm d}Y_{\rm A}^{(2)}(t)}{{\rm d}t} &= \frac{1}{2\tau_{\rm p}^{(2)}}(M_{\rm A}^{(2)}(t)-1)Y_{\rm A}^{(2)}(t)\\ &-Y_{\rm B}^{(2)}(t)(\eta_{\rm r}^{(2)}\sin\phi_{\rm BA}^{(2)}(t)+\eta_{\rm i}^{(2)}\cos\phi_{\rm BA}^{(2)}(t))\\ &-Y_{\rm C}^{(2)}(t)(\eta_{\rm r}^{(2)}\sin\phi_{\rm CA}^{(2)}(t)+\eta_{\rm i}^{(2)}\cos\phi_{\rm CA}^{(2)}(t))\\ &+k_{\rm r1}Y_{\rm A}^{(2)}(t-\tau_2)\cos(\phi_{\rm A}^{(2)}(t)\\ &+\omega_2\tau_2-\phi_{\rm A}^{(2)}(t-\tau_2))\\ &+k_{\rm inj}E_{\rm A}(t)\cos(\pi S_{\rm A}(t)-\phi_{\rm A}^{(2)}(t)),\end{aligned}\tag{8}$$

$$\begin{aligned}\frac{{\rm d}Y_{\rm B}^{(2)}(t)}{{\rm d}t} &= \frac{1}{2\tau_{\rm p}^{(2)}}(M_{\rm B}^{(2)}(t)-1)Y_{\rm B}^{(2)}(t)\\ &+Y_{\rm A}^{(2)}(t)(\eta_{\rm r}^{(2)}\sin\phi_{\rm BA}^{(2)}(t)-\eta_{\rm i}^{(2)}\cos\phi_{\rm BA}^{(2)}(t))\end{aligned}$$

$$
\begin{aligned}
&-Y_{\mathrm{C}}^{(2)}(t)(\eta_{\mathrm{r}2}^{(2)}\sin\phi_{\mathrm{CB}}^{(2)}(t)+\eta_{\mathrm{i}2}^{(2)}\cos\phi_{\mathrm{CB}}^{(2)}(t))\\
&+k_{\mathrm{r}2}Y_{\mathrm{B}}^{(2)}(t-\tau_2)\cos(\phi_{\mathrm{B}}^{(2)}(t)\\
&+\omega_2\tau_2-\phi_{\mathrm{B}}^{(2)}(t-\tau_2))\\
&+k_{\mathrm{inj}}E_{\mathrm{B}}(t)\cos(\pi S_{\mathrm{B}}(t)-\phi_{\mathrm{B}}^{(2)}(t)), \qquad (9)
\end{aligned}
$$

$$
\begin{aligned}
\frac{\mathrm{d}Y_{\mathrm{C}}^{(2)}(t)}{\mathrm{d}t} &= \frac{1}{2\tau_{\mathrm{p}}^{(2)}}(M_{\mathrm{C}}^{(2)}(t)-1)Y_{\mathrm{C}}^{(2)}(t)\\
&+Y_{\mathrm{A}}^{(2)}(t)(\eta_{\mathrm{r}}^{(2)}\sin\phi_{\mathrm{CA}}^{(2)}(t)-\eta_{\mathrm{i}}^{(2)}\cos\phi_{\mathrm{CA}}^{(2)}(t))\\
&+Y_{\mathrm{B}}^{(2)}(t)(\eta_{\mathrm{r}2}^{(2)}\sin\phi_{\mathrm{CB}}^{(2)}(t)-\eta_{\mathrm{i}2}^{(2)}\cos\phi_{\mathrm{CB}}^{(2)}(t))\\
&+k_{\mathrm{r}3}Y_{\mathrm{C}}^{(2)}(t-\tau_2)\cos(\phi_{\mathrm{C}}^{(2)}(t)\\
&+\omega_2\tau_2-\phi_{\mathrm{C}}^{(2)}(t-\tau_2))\\
&+k_{\mathrm{inj}}E_{\mathrm{C}}(t)\cos(\pi S_{\mathrm{C}}(t)-\phi_{\mathrm{B}}^{(2)}(t)), \qquad (10)
\end{aligned}
$$

$$
\frac{\mathrm{d}M_j^{(2)}(t)}{\mathrm{d}t} = \frac{1}{\tau_{\mathrm{n}}^{(2)}}[Q^{(2)}-M_j^{(2)}(t)(1+(Y_j^{(2)}(t))^2)], \qquad (11)
$$

$$
\begin{aligned}
\frac{\mathrm{d}\phi_{\mathrm{A}}^{(2)}(t)}{\mathrm{d}t} &= -\frac{\alpha_H^{(2)}}{2\tau_{\mathrm{p}}^{(2)}}(M_{\mathrm{A}}^{(2)}-1)+(\omega_2-\Omega_{\mathrm{A}})\\
&+\frac{Y_{\mathrm{B}}^{(2)}(t)}{Y_{\mathrm{A}}^{(2)}(t)}(\eta_{\mathrm{r}}^{(2)}\cos\phi_{\mathrm{BA}}^{(2)}(t)-\eta_{\mathrm{i}}^{(2)}\sin\phi_{\mathrm{BA}}^{(2)}(t))\\
&+\frac{Y_{\mathrm{C}}^{(2)}(t)}{Y_{\mathrm{A}}^{(2)}(t)}(\eta_{\mathrm{r}}^{(2)}\cos\phi_{\mathrm{CA}}^{(2)}(t)-\eta_{\mathrm{i}}^{(2)}\sin\phi_{\mathrm{CA}}^{(2)}(t))\\
&-k_{\mathrm{r}1}\frac{Y_{\mathrm{A}}^{(2)}(t-\tau_2)}{Y_{\mathrm{A}}^{(2)}(t)}\sin(\phi_{\mathrm{A}}^{(2)}(t)\\
&+\omega_2\tau_2-\phi_{\mathrm{A}}^{(2)}(t-\tau_2))\\
&-k_{\mathrm{inj}}\frac{E_{\mathrm{A}}(t)}{Y_{\mathrm{A}}^{(2)}(t)}\sin(\pi S_{\mathrm{A}}(t)-\phi_{\mathrm{A}}^{(2)}(t))-\Delta v, \qquad (12)
\end{aligned}
$$

$$
\begin{aligned}
\frac{\mathrm{d}\phi_{\mathrm{B}}^{(2)}(t)}{\mathrm{d}t} &= -\frac{\alpha_H^{(2)}}{2\tau_{\mathrm{p}}^{(2)}}(M_{\mathrm{B}}^{(2)}-1)+(\omega_2-\Omega_{\mathrm{B}})\\
&+\frac{Y_{\mathrm{A}}^{(2)}(t)}{Y_{\mathrm{B}}^{(2)}(t)}(\eta_{\mathrm{r}}^{(2)}\cos\phi_{\mathrm{BA}}^{(2)}(t)+\eta_{\mathrm{i}}^{(2)}\sin\phi_{\mathrm{BA}}^{(2)}(t))\\
&+\frac{Y_{\mathrm{C}}^{(2)}(t)}{Y_{\mathrm{B}}^{(2)}(t)}(\eta_{\mathrm{r}2}^{(2)}\cos\phi_{\mathrm{CB}}^{(2)}(t)-\eta_{\mathrm{i}2}^{(2)}\sin\phi_{\mathrm{CB}}^{(2)}(t))\\
&-k_{\mathrm{r}2}\frac{Y_{\mathrm{B}}^{(2)}(t-\tau_2)}{Y_{\mathrm{B}}^{(2)}(t)}\sin(\phi_{\mathrm{B}}^{(2)}(t)\\
&+\omega_2\tau_2-\phi_{\mathrm{B}}^{(2)}(t-\tau_2))\\
&-k_{\mathrm{inj}}\frac{E_{\mathrm{B}}(t)}{Y_{\mathrm{B}}^{(2)}(t)}\sin(\pi S_{\mathrm{B}}(t)-\phi_{\mathrm{B}}^{(2)}(t))-\Delta v, \qquad (13)
\end{aligned}
$$

$$
\begin{aligned}
\frac{\mathrm{d}\phi_{\mathrm{C}}^{(2)}(t)}{\mathrm{d}t} &= -\frac{\alpha_H^{(2)}}{2\tau_{\mathrm{p}}^{(2)}}(M_{\mathrm{C}}^{(2)}-1)+(\omega_2-\Omega_{\mathrm{C}})\\
&+\frac{Y_{\mathrm{A}}^{(2)}(t)}{Y_{\mathrm{C}}^{(2)}(t)}(\eta_{\mathrm{r}}^{(2)}\cos\phi_{\mathrm{CA}}^{(2)}(t)+\eta_{\mathrm{i}}^{(2)}\sin\phi_{\mathrm{CA}}^{(2)}(t))\\
&+\frac{Y_{\mathrm{B}}^{(2)}(t)}{Y_{\mathrm{C}}^{(2)}(t)}(\eta_{\mathrm{r}2}^{(2)}\cos\phi_{\mathrm{CB}}^{(2)}(t)+\eta_{\mathrm{i}2}^{(2)}\sin\phi_{\mathrm{CB}}^{(2)}(t))\\
&-k_{\mathrm{r}3}\frac{Y_{\mathrm{C}}^{(2)}(t-\tau_2)}{Y_{\mathrm{C}}^{(2)}(t)}\sin(\phi_{\mathrm{C}}^{(2)}(t)\\
&+\omega_2\tau_2-\phi_{\mathrm{C}}^{(2)}(t-\tau_2))\\
&-k_{\mathrm{inj}}\frac{E_{\mathrm{C}}(t)}{Y_{\mathrm{C}}^{(2)}(t)}\sin(\pi S_{\mathrm{C}}(t)-\phi_{\mathrm{C}}^{(2)}(t))-\Delta v, \qquad (14)
\end{aligned}
$$

where the superscripts 1 and 2 denote the TCL-SL_1 and TCL-SL_2, respectively; the subscripts A, B, and C represent lasers A, B, and C, respectively; the subscript $j=$ A, B, C (the same below); $Y_{\mathrm{A}}^{(1)}$, $Y_{\mathrm{B}}^{(1)}$, and $Y_{\mathrm{C}}^{(1)}$ are the normalized field amplitudes of the lasers A_1, B_1, and C_1, respectively. $Y_{\mathrm{A}}^{(2)}$, $Y_{\mathrm{B}}^{(2)}$, and $Y_{\mathrm{C}}^{(2)}$ are those of the laser A_2, B_2, and C_2, respectively; $M_{\mathrm{A}}^{(1)}$, $M_{\mathrm{B}}^{(1)}$, and $M_{\mathrm{C}}^{(1)}$ are the normalized carrier densities in the lasers A_1, B_1, and C_1 in turn. $M_{\mathrm{A}}^{(2)}$, $M_{\mathrm{B}}^{(2)}$, and $M_{\mathrm{C}}^{(2)}$ are those in the laser A_2, B_2, and C_2, respectively. $\phi_{\mathrm{A}}^{(1)}$, $\phi_{\mathrm{B}}^{(1)}$, and $\phi_{\mathrm{C}}^{(1)}$ are the phases of the lasers A_1, B_1, and C_1, respectively. $\phi_{\mathrm{A}}^{(2)}$, $\phi_{\mathrm{B}}^{(2)}$, and $\phi_{\mathrm{C}}^{(2)}$ are the phases of the laser A_2, B_2, and C_2 in turn. The phase differences $\phi_{\mathrm{BA}}^{(1),(2)}=\phi_{\mathrm{B}}^{(1),(2)}-\phi_{\mathrm{A}}^{(1),(2)}$, $\phi_{\mathrm{CA}}^{(1),(2)}=\phi_{\mathrm{C}}^{(1),(2)}-\phi_{\mathrm{A}}^{(1),(2)}$, and $\phi_{\mathrm{CB}}^{(1),(2)}=\phi_{\mathrm{C}}^{(1),(2)}-\phi_{\mathrm{B}}^{(1),(2)}$. The term $\eta^{(1)}$ is the complex coupling coefficient between the lasers A_1 and B_1, which is identical to those between the lasers A_1 and C_1. The $\eta^{(2)}$ is the complex coupling coefficient between the lasers A_2 and B_2, which is the same with those between the lasers A_2 and C_2. $\eta_{\mathrm{r}}^{(1)}$ and $\eta_{\mathrm{i}}^{(1)}$ are the real and imaginary parts of $\eta^{(1)}$, respectively. $\eta_{\mathrm{r}}^{(2)}$ and $\eta_{\mathrm{i}}^{(2)}$ are the real and imaginary parts of $\eta^{(2)}$. $\eta^{(1)}$ and $\eta^{(2)}$ are defined as

$$
\begin{aligned}
&\left|\eta^{(1)}\right| = C_\eta\exp\left(-2W_{\mathrm{r}}\frac{d^{(1)}}{a}\right),\\
&\arg(\eta^{(1)}) = C_\theta-2W_{\mathrm{i}}\frac{d^{(1)}}{a}, \qquad (15)\\
&\left|\eta^{(2)}\right| = C_\eta\exp\left(-2W_{\mathrm{r}}\frac{d^{(2)}}{a}\right),\\
&\arg(\eta^{(2)}) = C_\theta-2W_{\mathrm{i}}\frac{d^{(2)}}{a}, \qquad (16)
\end{aligned}
$$

where W_{r}, W_{i} are the real and imaginary parts of the transverse propagation constant in the regions outside the core of LWGs A, B, and C in the TCL-SL_1 or the TCL-SL_2. C_η, C_θ can be found from numerical integration. $\eta_{\mathrm{r}2}^{(1)}$ and $\eta_{\mathrm{i}2}^{(1)}$ are the real and imaginary parts of the complex coupling coefficient $\eta_2^{(1)}$ between the lasers B_1 and C_1. $\eta_{\mathrm{r}2}^{(2)}$ and $\eta_{\mathrm{i}2}^{(2)}$ are the real and imaginary parts of $\eta_2^{(2)}$ between the lasers B_2 and C_2. $\eta_2^{(1)}$ and

$\eta_2^{(2)}$ are expressed as

$$\left|\eta_2^{(1)}\right| = C_\eta \exp\left(-2W_\mathrm{r}\frac{2d^{(1)}+a}{a}\right),$$
$$\arg\left(\eta_2^{(1)}\right) = C_\theta - 2W_\mathrm{i}\frac{2d^{(1)}+a}{a}, \tag{17}$$
$$\left|\eta_2^{(2)}\right| = C_\eta \exp\left(-2W_\mathrm{r}\frac{2d^{(2)}+a}{a}\right),$$
$$\arg\left(\eta_2^{(2)}\right) = C_\theta - 2W_\mathrm{i}\frac{2d^{(2)}+a}{a}. \tag{18}$$

Moreover, τ is the self-feedback delay; $k_{\mathrm{f}1}$, $k_{\mathrm{f}2}$, and $k_{\mathrm{f}3}$ are the self-feedback strengths of lasers A_1, B_1, and C_1 in turn; $k_{\mathrm{r}1}$, $k_{\mathrm{r}2}$, and $k_{\mathrm{r}3}$ are the feedback strengths for the delay lines DL_1, DL_2, and DL_3, respectively; k_{inj} is injection strength. $\tau_\mathrm{n}^{(1)}$ and $\tau_\mathrm{n}^{(2)}$ are the carrier lifetime; $\tau_\mathrm{p}^{(1)}$ and $\tau_\mathrm{p}^{(2)}$ are the photon lifetime; $\alpha_\mathrm{H}^{(1)}$ and $\alpha_\mathrm{H}^{(2)}$ are the line-width enhancement factor that accounts for the phase-amplitude coupling in the electric field; ω_1 and ω_2 are the free-running angular frequencies of the total electric field of the TCL-SL_1 and TCL-SL_2, respectively; Ω_A, Ω_B, and Ω_C are respectively the waveguide frequencies of LWGs A, B, and C in the TCL-SL_1 or the TCL-SL_2. The term $\Delta\nu$ is the frequency detuning between D-SL and TCL-SL_2. $Q^{(1)}$ and $Q^{(2)}$ are the normalized pumping rate, which can be expressed in terms of the ratio of pumping rate to its threshold value, P/P_th, as

$$Q^{(1),(2)} = C_Q\left(\frac{P^{(1),(2)}}{P_\mathrm{th}} - 1\right) + \frac{P^{(1),(2)}}{P_\mathrm{th}}, \tag{19}$$

where $C_Q = a_\mathrm{diff}N_0/g_\mathrm{th}$, with a_diff as the differential gain, N_0 as the carrier density under transparency, and g_th as the unit length gain under threshold. The injected slowly varying complex electric field $E_j(t)$ can be written as

$$E_j(t) = E_\mathrm{d}\sqrt{\frac{ca_\mathrm{diff}\tau_\mathrm{n}^{(2)}}{n_0}}, \tag{20}$$

where E_d is the amplitude of CW output from the D-SL; c is the speed of light in vacuum; n_0 is the refractive index of the laser waveguides A, B, and C in the TCL-SL_2. The j-th masked input signal $S_j(t)$ is multiplied by the j-th input data u_j (n'_j), the mask signal, the j-th modulated signal and the scaling factor γ, which can be expressed as

$$S_j(t) = \mathrm{Mask}(t)\times u_j\left(n'_j\right)\times m_j\left(n'_j\right)\times\gamma, \tag{21}$$

where the term Mask is chaos signal and presented in Ref. [49]. In these three input data, $k_\mathrm{A} = \tau_\mathrm{A}/h$, $k_\mathrm{B} = \tau_\mathrm{B}/h$, and $k_\mathrm{C} = \tau_\mathrm{C}/h$. h is the step size. τ_A is the channel delay between the TA_1 and RA_1. τ_B is that between the TA_2 and RA_2. τ_C is that between the TA_3 and RA_3.

As displayed in Fig. 1, although the values of the delay lengths k_A, k_B, and k_C are related to the measured distances, and theoretically unknown, but the values of these three probe signals (u_A (n'_A), u_B (n'_B), and u_C (n'_C)) can be obtained by using the RAs and DMs. u_A (n'_A), u_B (n'_B), and u_C (n'_C) are injected into the RC by the PMs. According to lag chaotic synchronization theory,[22,49] we obtain lag synchronous solutions as

$$y_j(n) = u_j(n'_j),\quad j = \mathrm{A},\ \mathrm{B},\ \mathrm{C}, \tag{22}$$

where the time-dependent output $y_j(n)$ is taken to be a linear function of the j-th reservoir state and input data such that

$$y_j(n) = W_{j,1}b_\mathrm{out} + W_{j,2}u_j(n'_j) + \sum_{\mathrm{i}=1}^{N} W_{j,i+2}Y_{j,i}^{(2)}(n), \tag{23}$$

where $W_{j,i}$ is the i-th-element of the output weight matrix $\boldsymbol{W}_j$; the variable $Y_{j,i}^{(2)}(n)$ is the i-th internal states of the j-th reservoir R_j; the term b_out is a constant and equal to 1. Previous studies have shown that $\boldsymbol{W}_j$ can be analytically given by[32]

$$\boldsymbol{W}_j = \boldsymbol{Z}_j\boldsymbol{X}_j^\mathrm{T}/(\boldsymbol{X}_j\boldsymbol{X}_j^\mathrm{T} + \lambda\boldsymbol{\Pi}), \tag{24}$$

where the superscript T denotes transpose; $\boldsymbol{\Pi}$ is an identity matrix; λ is the ridge regression parameter for avoiding overfitting and set as 10^{-6}; $\boldsymbol{X}_j$ is the matrix whose k-th column is $[b_\mathrm{out}; u_j(k-k_j); Y_{j,i}^{(2)}(k)]$ and $\boldsymbol{Z}_j$ is the matrix whose k-th column is $[u_j(k-k_j+1)]$.

In this scheme, three microwave signals are considered as sine waves and expressed by

$$m_j(n) = A\sin(\omega_j n), \tag{25}$$

where ω_j is the angular frequency of the j-th microwave signal; and A is the amplitude. By using the synchronous division presented in Fig. 1, these three-channel decoding microwave signals can be obtained by

$$m'_j(n) = \frac{u_j(n'_j)m_j(n'_j)}{y_j(n)}. \tag{26}$$

Under three lag synchronization solutions (see Eq. (22)), these decoding microwave signals are derived from Eqs. (25) and (26) as follows:

$$m'_j(n) = A\sin(\omega_j(n-k_j)). \tag{27}$$

According to Hilbert transform, the analytic signal of $m_j(t)$ is written as

$$\psi_j(n) = m_j(n) + j\widetilde{m}_j(n), \tag{28}$$

where $\widetilde{m}_j(n)$ is the Hilbert transform of $m_j(n)$. Based on Eq. (28), the phase of $m_j(n)$ is given as follows:

$$\phi_{m_j}(n) = \arctan\frac{\widetilde{m}_j(n)}{m_j(n)} = \omega_j n. \tag{29}$$

Similarly, the phase of $\widetilde{m}'_j(n)$ is given as follows:

$$\phi'_{m_j}(n) = \arctan\frac{\widetilde{m}'_j(n)}{m'_j(n)} = \omega_j(n-k'_j). \tag{30}$$

According to Eqs. (29) and (30), the channel delay time for the j-th target T_j is written as

$$\tau_j = \frac{\phi_{m_j}(n) - \phi'_{m_j}(n)}{\omega_j} = \frac{\Delta\phi_{m_j}h}{\omega_j}, \tag{31}$$

and the distance of these three targets can be derived as

$$d_{\rm A} = \frac{\tau_{\rm A}c}{2},\ d_{\rm B} = \frac{\tau_{\rm B}c}{2},\ d_{\rm C} = \frac{\tau_{\rm C}c}{2}, \tag{32}$$

where c is the speed of light in vacuum.

3. Results and discussion

The key material parameter values for the TCL-SL$_1$ and TCL-SL$_2$ are identical and given as follows:[51] $g_{\rm th} = 87.7\ {\rm cm}^{-1}$; $W_{\rm r} = 1.26$, $W_{\rm i} = 0$; $C_\eta = 83.6\ {\rm ns}^{-1}$, $C_\theta = 0$, $n_0 = 3.4$. The half-width (a) of each LWG in the TCL-SL$_1$ or TCL-SL$_2$ is taken as 4 μm. The other parameter values for calculation are given as follows:[41,51] $a_{\rm diff} = 1\times10^{-15}\ {\rm cm}^2$; $N_0 = 1\times10^{18}\ {\rm cm}^{-3}$; $k_{\rm inj} = 12.43\ {\rm ns}^{-1}$; $\Delta\nu = -4$ GHz and $E_{\rm d} = 2.5612\times10^{10}$ V/m; $\tau_{\rm n}^{(1)}$, $\tau_{\rm n}^{(2)} = 1.0$ ns; $\tau_{\rm p}^{(1)}$, $\tau_{\rm p}^{(2)} = 1.53$ ps; $\alpha_{\rm H}^{(1)} = 3$, $\alpha_{\rm H}^{(2)} = 2$; $k_{\rm f1}$, $k_{\rm f2}$, $k_{\rm f3} = 3\ {\rm ns}^{-1}$; $k_{\rm r1}$, $k_{\rm r2}$, $k_{\rm r3} = 7\ {\rm ns}^{-1}$; $d^{(1)}/a = 1.2$, $d^{(2)}/a = 3.5$; $P^{(1)}/P_{\rm th} = 1.2$, $P^{(2)}/P_{\rm th} = 1.4$. The waveguide frequencies $\Omega_{\rm A}$, $\Omega_{\rm B}$, and $\Omega_{\rm C}$ are all equal to 1.4499×10^{15} rad/s, where central wavelengths are all 1310 nm.

We calculate numerically Eqs. (1)–(14) by using the four-order Runge–Kutta method with a step h of 1 ps. For the numerically solving Eqs. (1)–(7) for the TCL-SL$_1$, 6000 samples of input data are recorded under the sampling interval of 10 ps. After discarding the first 1000 samples (to eliminate transient states), we use the 3000 points for training the three reservoirs (R_A, R_B, and R_C), and take their remaining 2000 points to test these reservoirs. Moreover, three mask signals are all chaotic signals generated by two mutually-coupled SLs, as presented in Ref. [49]. The intervals of these mask signals are all denoted by θ and set to 20 ps. The amplitudes of the mask signals are adjusted, making their standard deviations to be 1 and mean values of 0. The period T of the input data is set as 8 ns, and hence the data processing speed is 125 Mb/s. The number of virtual nodes N is considered as 400, where $N = T/\theta$. The delay time $\tau_2 = T + \theta$. The scaling factor γ is set as 1.

For the prediction tasks of the nonlinear dynamics of the lasers A$_1$, B$_1$, and C$_1$, the training error, i.e., the j-th normalized mean-square error (NMSE$_j$) between the j-th input data ($u_j(n-k_j)$) and the j-th reservoir (R$_j$) output $y_j(n)$, is calculated to measure the performance of the R$_j$, which is defined as

$${\rm NMSE}_j = \frac{1}{L}\frac{\sum_{n=1}^{L}(y_j(n)-u_j(n'_j))^2}{{\rm var}(y_j(n))}, \tag{33}$$

where L is the total number of data in the testing data set; the term var represents the variance. The NMSE with subscripts of j indicates how far the time series $y_j(n)$ generated by the j-th reservoir (R_j) deviates from the j-th delayed time series $u_j(n'_j)$. NMSE$_j = 0$ means that $y_j(n)$ is perfectly matched with $u_j(n'_j)$. When NMSE$_j = 1$ indicates that they are no similarities at all. Moreover, while NMSE$_j$ is less than 0.1, the trained reservoirs (R_A, R_B and R_C) can infer the output chaotic trajectories from the lasers A$_1$, B$_1$, and C$_1$, respectively. In other words, the j-th delayed input time series $u_j(n'_j)$ from the laser-j element in the TCL-SL$_1$ wishes to synchronize with the trained predicted values $y_j(n)$ from the R$_j$ output, which can be characterized by using the correlation coefficient as follows:

$$\rho_j = \frac{\left\langle\left[I_j^{(1)}(n'_j) - \left\langle I_j^{(1)}(n'_j)\right\rangle\right]\left[I_j^{(2)}(n) - \left\langle I_j^{(2)}(n)\right\rangle\right]\right\rangle}{\left\langle\left[I_j^{(1)}(n'_j) - \left\langle I_j^{(1)}(n'_j)\right\rangle\right]^2\right\rangle^{1/2}\left\langle\left[I_j^{(2)}(n) - \left\langle I_j^{(2)}(n)\right\rangle\right]^2\right\rangle^{1/2}}, \tag{34}$$

where $I_j^{(1)} = |u_j(n'_j)|^2$ and $I_j^{(2)} = \left|y_j(n)\right|^2$. The symbol $\langle\ \rangle$ denotes the time average. Note that ρ ranges from -1 to 1. With the bigger value of ρ, the higher quality of synchronization can be obtained. When ρ is equal to ±1, the in-phase and anti-phase synchronous solutions exist in the system.

3.1. Training errors for the chaotic dynamics

To observe the similarity of the output of the driving laser-element in the TCL-SL$_1$ to the corresponding trained reservoir output, figure 2 displays the samples of the target chaotic time series data ($u_A(n'_A)$, $u_B(n'_B)$, and $u_C(n'_C)$), and the output of the reservoirs (R_A, R_B, and R_C). Here, $\tau_A = 10$ ns; $\tau_B = 15$ ns; $\tau_C = 20$ ns; $\alpha_H^{(1)} = 3$; $\alpha_H^{(2)} = 2$; k_{f1}, k_{f2}, $k_{f3} = 3\ {\rm ns}^{-1}$; k_{r1}, k_{r2}, $k_{r3} = 7\ {\rm ns}^{-1}$; $d^{(1)}/a = 1.2$; $d^{(2)}/a = 3.5$; $P^{(1)}/P_{\rm th} = 1.2$, $P^{(2)}/P_{\rm th} = 1.4$; $T = 8$ ns; $\theta = 20$ ps; $\gamma = 1$; $\tau_2 = 8.02$ ns, and $k_{\rm inj} = 12.43\ {\rm ns}^{-1}$. As seen from Fig. 2(a), the trajectory of $u_A(n'_A)$ is highly similar to that of $y_A(n)$. The NMSE between them is 0.054 when $\tau_2 = 8.02$ ns and $\theta = 20$ ps (see Figs. 3(a) and 4(a)). As further observed from Figs. 2(b) and 2(c), the traces of $u_B(n'_B)$ and $u_C(n'_C)$ from lasers B$_1$ and C$_1$

output are almost identical to those of $y_B(n)$ and $y_C(n)$, respectively. The NMSE between $u_B(n'_B)$ and $y_B(n)$ and that between $u_C(n'_C)$ and $y_C(n)$ are 0.053 and 0.052, respectively, when $\tau_2 = 8.02$ ns and $\theta = 20$ ps (see Figs. 3 and 4). These indicate that the trained reservoirs R_A, R_B, and R_C can accurately infer the chaotic trajectories of the delayed probe signals $u_A(n'_A)$, $u_B(n'_B)$, and $u_C(n'_C)$, respectively.

To further explore the predictive performances of three parallel trained reservoirs to the chaotic trajectories of three-channel delayed probe signals. Figure 3 displays three training errors ($NMSE_A$, $NMSE_B$ and $NMSE_C$) as a function of the delay-time τ_2 under $\theta = 20$ ps, $\tau_A = 10$ ns, $\tau_B = 15$ ns, and $\tau_C = 20$ ns. It can be clearly seen from Fig. 3 that in the region of τ_2 between 1 ns and 10 ns, these training errors are less than 0.065, but they show a rise in oscillation with the increase of τ_2. The reason that a longer delay-time τ_2 results in an oscillation rising training error may be explained as follows. In this work, when θ is fixed at 20 ps, $T = \tau_2 - \theta$ and $N = \tau_2/\theta - 1$, a larger N is accompanied by a larger τ_2, indicating that a higher dimension state space. In such a case, the predictions of the trained reservoirs to the delayed probe signals becomes unstable and more difficult, resulting in a larger NMSE. Moreover, for the prediction of three-channel delayed probe signals, figure 4 shows their training errors as a function of the virtual node interval θ. One sees from this figure that with T fixed at 8 ns, these three training errors appear in a cliff-like decline when θ increases from 4 ps to 12 ps, then gradually stabilize to 0.0474 with the increase of θ from 12 ps to 200 ps. The reason is explained as follows: a small θ induces to the reduction of the trained reservoirs response, showing larger training errors. As θ increases from 15 ps to 200 ps, the response of the trained reservoir will be further enhanced, resulting in less training errors. In addition, although the dimension of the state space further decreases with the increase of θ, there are still enough virtual nodes for training reservoir, making these training errors small and varied between 0.0474 and 0.055.

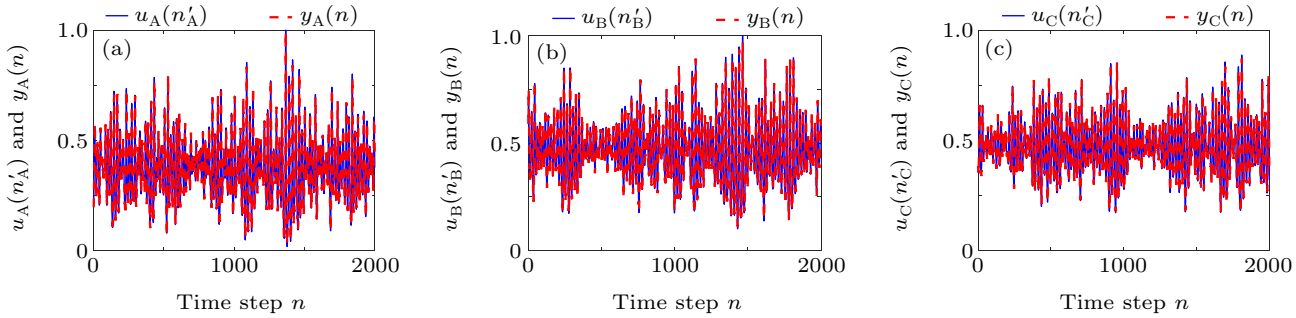


Fig. 2. (a) A sample of the delayed chaotic time series data $u_A(n'_A)$ (the blue solid line) and $y_A(n)$ (the red dashed line). (b) A sample of the delayed chaotic time series data $u_B(n'_B)$ (the blue solid line) and $y_B(n)$ (the red dashed line). (c) A sample of the delayed chaotic time series data $u_C(n'_C)$ (the blue solid line) and $y_C(n)$ (the red dashed line). Here, $\tau_A = 10$ ns; $\tau_B = 15$ ns; $\tau_C = 20$ ns; $\alpha_H^{(1)} = 3$; $\alpha_H^{(2)} = 2$; k_{f1}, k_{f2}, $k_{f3} = 3$ ns^{-1}; k_{r1}, k_{r2}, $k_{r3} = 7$ ns^{-1}; $d^{(1)}/a = 1.2$; $d^{(2)}/a = 3.5$; $P^{(1)}/P_{th} = 1.2$, $P^{(2)}/P_{th} = 1.4$; $T = 8$ ns; $\theta = 20$ ps; $\gamma = 1$; $\tau_2 = 8.02$ ns and $k_{inj} = 12.43$ ns^{-1}.

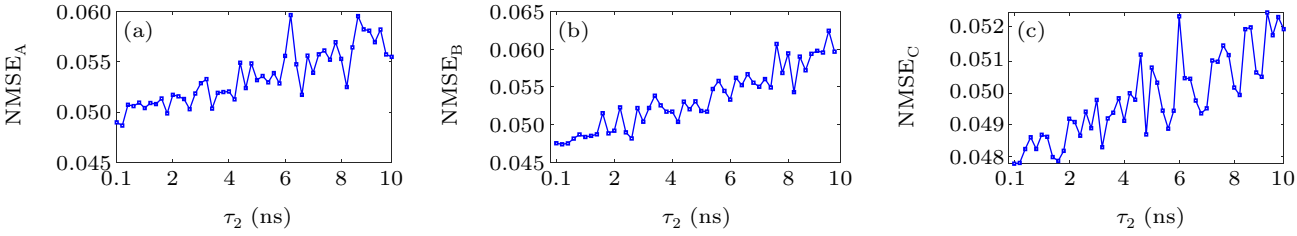


Fig. 3. (a) The $NMSE_A$ as a function of the delay-time τ_2 for the prediction of the trained reservoir R_A to $u_A(n'_A)$; (b) the $NMSE_B$ as a function of τ_2 for the prediction of the trained reservoir R_B to $u_B(n'_B)$; (c) the $NMSE_C$ as a function of τ_2 for the prediction of the reservoir R_C to $u_C(n'_C)$. Here, $\tau_A = 10$ ns; $\tau_B = 15$ ns; $\tau_C = 20$ ns and other parameters except for τ_2 are the same as those in Fig. 2.

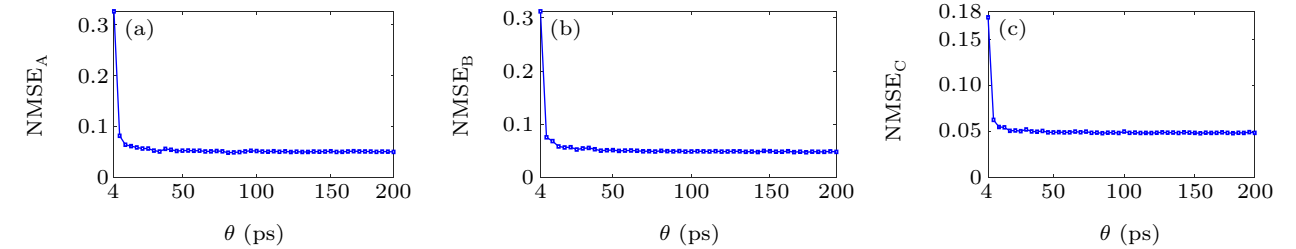


Fig. 4. (a) The $NMSE_A$ as a function of the virtual node interval θ for the prediction of the trained reservoir R_A to $u_A(n'_A)$; (b) the $NMSE_B$ as a function of θ for the prediction of the trained reservoir R_B to $u_B(n'_B)$; (c) the $NMSE_C$ as a function of θ for the prediction of the reservoir R_C to $u_C(n'_C)$. Here, $\tau_A = 10$ ns; $\tau_B = 15$ ns; $\tau_C = 20$ ns and other parameters except for θ are the same as those in Fig. 2.

3.2. Predictive learning of three-channel lag chaotic synchronizations

As displayed in Figs. 2–4, three trained reservoir computers based on the driving lasers A_2, B_2, and C_2 can reproduce the trajectories of three-channel delayed probe signals, respectively. Their training errors are very small if θ is more than 15 ps and τ_2 is less than 10 ns. These results indicate that the trained reservoirs can be well synchronized with three-channel delayed probe signals. To further look into the quality of their synchronization, we present the evolutions of the correlation coefficients (ρ_A, ρ_B, and ρ_C) in the parameter spaces of τ and τ_A, τ and τ_B, τ and τ_C, γ and τ_2, as shown in Fig. 5. Here, $\alpha_H^{(1)} = 3$; $\alpha_H^{(2)} = 2$; $k_{f1}, k_{f2}, k_{f3} = 3\ \text{ns}^{-1}$; $k_{r1}, k_{r2}, k_{r3} = 7\ \text{ns}^{-1}$; $d^{(1)}/a = 1.2$; $d^{(2)}/a = 3.5$; $P^{(1)}/P_{th} = 1.2$, $P^{(2)}/P_{th} = 1.4$; $T = 8$ ns and $\theta = 20$ ps. From Figs. 5(a1)–5(c1), when τ is between 3 ns and 9 ns, it is found that ρ_A, ρ_B, and ρ_C are all more than 0.971 in the parameter spaces of τ and τ_A, τ and τ_B, τ and τ_C. As seen from Figs. 5(a2)–5(c2), these correlation coefficients are more than 0.971 when γ ranges from 0.2 to 1 and τ_2 varies from 1ns to 9 ns. In particular, with the further increases of the feedback time τ_2, ρ_A, ρ_B, and ρ_C gradually decrease owing to the slow increase of corresponding training errors (see Fig. 5).

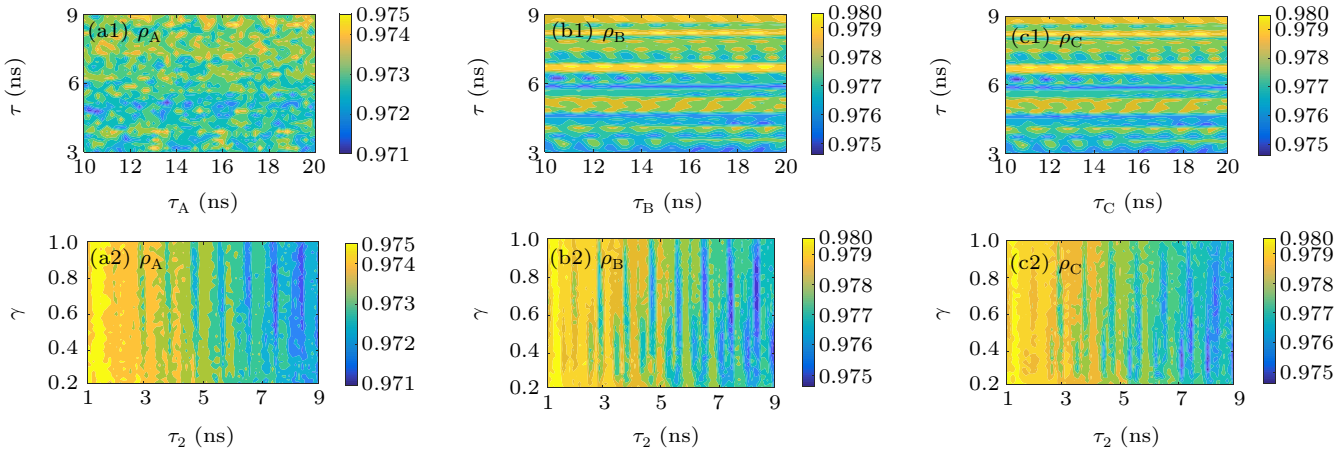


Fig. 5. Maps of the evolutions of the correlation coefficients (ρ_A, ρ_B, and ρ_C) in different parameter spaces. Here, $\alpha_H^{(1)} = 3$; $\alpha_H^{(2)} = 2$; $k_{f1}, k_{f2}, k_{f3} = 3\ \text{ns}^{-1}$; $k_{r1}, k_{r2}, k_{r3} = 7\ \text{ns}^{-1}$; $d^{(1)}/a = 1.2$; $d^{(2)}/a = 3.5$; $P^{(1)}/P_{th} = 1.2$, $P^{(2)}/P_{th} = 1.4$; $T = 8$ ns and $\theta = 20$ ps. (a1) The parameter space of τ and τ_A where $\gamma = 1$, $\tau_2 = 8.02$ ns; (b1) that of τ and τ_B where $\gamma = 1$, $\tau_2 = 8.02$ ns; (c1) that of τ and τ_C where $\gamma = 1$, $\tau_2 = 8.02$ ns; (a2)–(c2) the parameter space of γ and the reservoir delay time τ_2 where $\tau = 4$ ns, $\tau_A = 10$ ns, $\tau_B = 15$ ns and $\tau_C = 20$ ns.

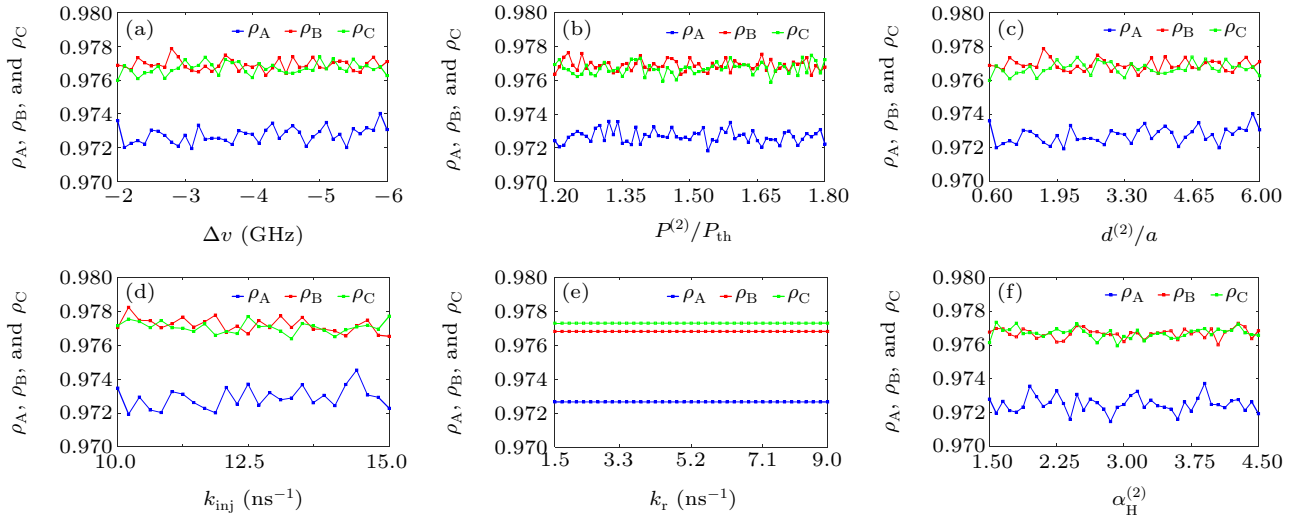


Fig. 6. Dependences of the correlation coefficients (ρ_A, ρ_B, and ρ_C) on the other key parameters, such as Δv, $P^{(2)}/P_{th}$, $d^{(2)}/a$, k_{inj}, k_r, and $\alpha_H^{(2)}$, when the other parameter values are given in Fig. 2. Here, (a) ρ_A, ρ_B, and ρ_C versus Δv; (b) ρ_A, ρ_B, and ρ_C versus $P^{(2)}/P_{th}$ under $P^{(1)}/P_{th} = 1.2$; (c) ρ_A, ρ_B, and ρ_C versus $d^{(2)}/a$ under $d^{(1)}/a = 1.2$; (d) ρ_A, ρ_B, and ρ_C versus k_{inj}; (e) ρ_A, ρ_B, and ρ_C versus k_r, where $k_r = k_{r1}, k_{r2}, k_{r3}$ and $k_{f1}, k_{f2}, k_{f3} = 3\ \text{ns}^{-1}$; (f) ρ_A, ρ_B, and ρ_C versus $\alpha_H^{(2)}$ under $\alpha_H^{(1)} = 3$.

In order for even further observation of the influences of the other parameters on these synchronization qualities, figure 6 presents the dependences of the correlation coefficients on some key parameters, such as Δv, $P^{(2)}/P_{th}$, $d^{(2)}/a$, k_{inj}, k_{r1}, k_{r2}, k_{r3}, and $\alpha_H^{(2)}$, when $k_{f1}, k_{f2}, k_{f3} = 3\ \text{ns}^{-1}$, $\alpha_H^{(1)} = 3$, $d^{(1)}/a = 1.2$, $P^{(1)}/P_{th} = 1.2$ and other parameter values are given in Fig. 2. As displayed in Fig. 6(a), when Δv is between -2 GHz and -6 GHz, ρ_A appears a slight oscillation

change from 0.972 to 0.974. $\rho_{\rm B}$ slightly varies from 0.9762 to 0.978, and $\rho_{\rm C}$ varies from 0.976 to 0.9777. As seen from Fig. 6(b) where $P^{(2)}/P_{\rm th}$ varies from $0.5P^{(1)}/P_{\rm th}$ to $1.5P^{(1)}/P_{\rm th}$ (1.2 to 1.8), $\rho_{\rm A}$ shows a slight oscillation between 0.972 and 0.9738. $\rho_{\rm B}$ appears a slight change from 0.9765 to 0.9778, and $\rho_{\rm C}$ shows a slight variation from 0.976 to 0.9777. When $d^{(2)}/a$ is between $0.5d^{(1)}/a$ and $5d^{(1)}/a$ (0.6 and 6), it is found from Fig. 6(c) that $\rho_{\rm A}$ slightly changes from 0.972 to 0.9741, $\rho_{\rm B}$ slightly varies from 0.9763 to 0.978, and $\rho_{\rm C}$ slightly varies from 0.976 to 0.9772. With the increase of $k_{\rm inj}$ from 10 ns^{-1} and 15 ns^{-1}, one sees from Fig. 6(d) that $\rho_{\rm A}$ slightly oscillates between 0.9719 and 0.975, $\rho_{\rm B}$ appears a slight oscillation between 0.9763 and 0.9782, and $\rho_{\rm C}$ shows a slight oscillation between 0.9762 and 0.9779. As seen from Fig. 6(e) where $k_{\rm r} = k_{\rm r1}$, $k_{\rm r2}$, $k_{\rm r3}$, when it varies from $0.5k_{\rm f1}$ to $3k_{\rm f1}$ (1.5 ns^{-1} to 9 ns^{-1}), $\rho_{\rm A}$, $\rho_{\rm B}$, and $\rho_{\rm C}$ all keep unchanged, and their values are kept at 0.9728, 0.9769, and 0.9773, respectively. As displayed in Fig. 6(f), with the range of $\alpha_{\rm H}^{(2)}$ from $0.5\alpha_{\rm H}^{(1)}$ to $1.5\alpha_{\rm H}^{(1)}$ (1.5 to 4.5), $\rho_{\rm A}$ shows a slight variation from 0.9716 to 0.974, $\rho_{\rm B}$ appears a slight change from 0.976 to 0.9773, and $\rho_{\rm C}$ shows a slight oscillation between 0.9761 and 0.9776.

These findings from Figs. 5 and 6 show that even when there are mismatches between some key parameters of the driving laser-element and the response laser-element (reservoir), high-quality lag chaotic synchronization between one-channel delayed probe signal and its corresponding trained RC can still be achieved. The reason is that under very small training errors, these three well-trained RCs can accurately infer the chaotic trajectories of three-channel delayed probe signals, respectively.

3.3. Synchronized chaotic lidar ranging to multi-target

In the following, under high-quality lag chaotic synchronizations of three channel delayed probe signals presented in Fig. 5 by using the delayed-based reservoir computing approach, we utilize three-channel synchronized probe signals for the ranging to the targets $\rm T_A$, $\rm T_B$, and $\rm T_C$. For the verification of the reliability and accuracy of the ranging to these three targets, the actual distances of these targets are set as $d_{T_{\rm A}} = 1.5$ m, $d_{T_{\rm B}} = 2.25$ m, and $d_{T_{\rm C}} = 3$ m. From these distances, we obtain three corresponding channel-delays as $\tau_{\rm A} = 10$ ns, $\tau_{\rm B} = 15$ ns, and $\tau_{\rm C} = 20$ ns. In addition, the angular frequencies of three sinusoidal waves ($m_{\rm A}$, $m_{\rm B}$, and $m_{\rm C}$) are taken as $\omega_{\rm A} = 2\pi/4\tau_{\rm A}$, $\omega_{\rm B} = 2\pi/4\tau_{\rm B}$, and $\omega_{\rm C} = 2\pi/4\tau_{\rm C}$. For these target distances as mentioned above, Figure 7 presents the temporal traces of the phases of these sinusoidal waves and their corresponding decoding signals ($m'_{\rm A}$, $m'_{\rm B}$, and $m'_{\rm C}$). Here, $\phi_{m_{\rm A}}$, $\phi_{m_{\rm B}}$, and $\phi_{m_{\rm C}}$ are the phases of $m_{\rm A}$, $m_{\rm B}$, and $m_{\rm C}$, respectively; $\phi'_{m_{\rm A}}$, $\phi'_{m_{\rm B}}$, and $\phi'_{m_{\rm C}}$ are the phases of $m'_{\rm A}$, $m'_{\rm B}$, and $m'_{\rm C}$, respectively. From Fig. 7, it is found that all phases show an approximately linear increase in periodicity when the targets $\rm T_A$, $\rm T_B$ and $\rm T_C$ locate in different distances, respectively. Moreover, the phase differences $\Delta\phi_{m_{\rm A}}(\phi_{m_{\rm A}} - \phi'_{m_{\rm A}})$, $\Delta\phi_{m_{\rm B}}(\phi_{m_{\rm B}} - \phi'_{m_{\rm B}})$ and $\Delta\phi_{m_{\rm C}}(\phi_{m_{\rm C}} - \phi'_{m_{\rm C}})$ almost remains unchanged at any time. Using these phase differences from Figs. 7(a)–7(c) and Eqs. (31)–(32), we calculate the temporal traces of the distances to be measured ($d_{\rm A}$, $d_{\rm B}$, and $d_{\rm C}$), as displayed in Fig. 8. It is found from this figure that $d_{\rm A}$ slightly ranges from 1.462 m to 1.55 m under $d_{T_{\rm A}} = 1.5$ m; $d_{\rm B}$ slowly varies between 2.196 m and 2.335 m when $d_{T_{\rm B}} = 2.25$ m; $d_{\rm C}$ slightly oscillates between 2.891 m and 3.179 m while $d_{T_{\rm C}} = 3$ m. In addition, for the ranging to the targets $\rm T_A$, $\rm T_B$, and $\rm T_C$, the expressions $|\langle d_{\rm A}\rangle - d_{T_{\rm A}}|$, $|\langle d_{\rm B}\rangle - d_{T_{\rm B}}|$ and $|\langle d_{\rm C}\rangle - d_{T_{\rm C}}|$ are taken as the absolute errors $|\Delta d_{\rm A}|$, $|\Delta d_{\rm B}|$, and $|\Delta d_{\rm C}|$, respectively. According to these three expressions, we obtain that $|\Delta d_{\rm A}| = 0.17$ mm, $|\Delta d_{\rm B}| = 0.43$ mm and $|\Delta d_{\rm C}| = 0.64$ mm. These results indicate that all absolute errors of the ranging to these targets can reach millimeter magnitude.

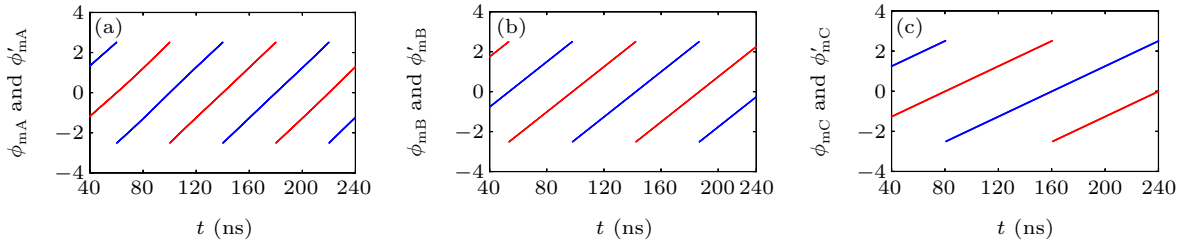


Fig. 7. (a) Time traces of the phases $\phi_{m_{\rm A}}$ and $\phi'_{m_{\rm A}}$; (b) those of the phases $\phi_{m_{\rm B}}$ and $\phi'_{m_{\rm B}}$; and (c) those of the phases. Here, $\tau_{\rm A} = 10$ ns, $\tau_{\rm B} = 15$ ns, $\tau_{\rm C} = 20$ ns and other parameters are the same as those in Fig. 2.

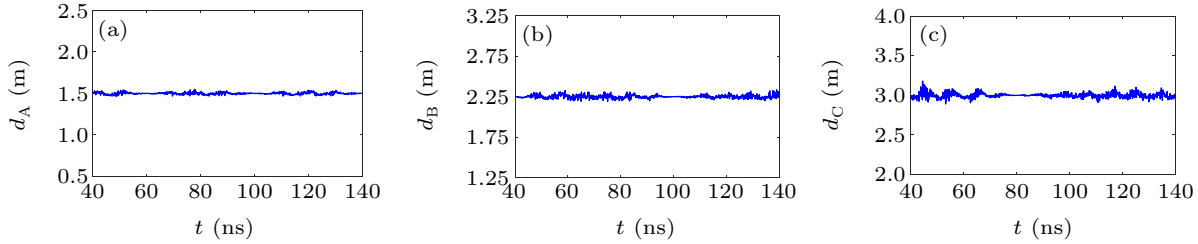


Fig. 8. (a) The temporal trace of the measured distance $d_{\rm A}$ for the target $\rm T_A$; (b) that of the measured distance $d_{\rm B}$ for the target $\rm T_B$; and (c) that of the measured distance $d_{\rm C}$ for the target $\rm T_C$. Here, $\tau_{\rm A} = 10$ ns, $\tau_{\rm B} = 15$ ns, $\tau_{\rm C} = 20$ ns and other parameters are the same as those in Fig. 2.

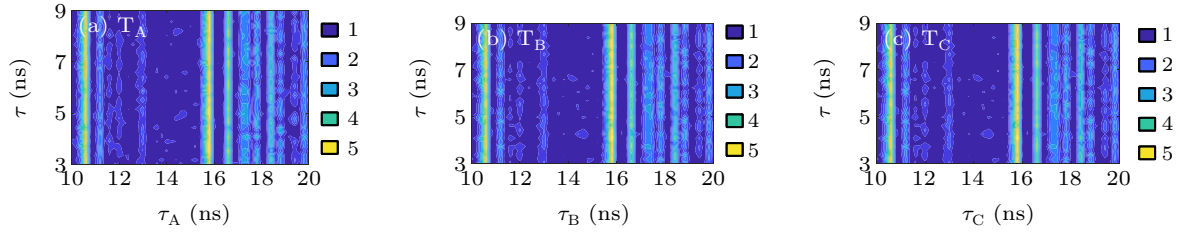


Fig. 9. Maps of the three relative errors evolutions in the parameter space of τ and τ_A (τ_B or τ_C). Here, (a) RE_A; (b) RE_B; (c) RE_C. State 1: $0 < RE_j \leq 0.1\%$ and dark-blue; state 2: $0.1\% < RE_j \leq 0.2\%$ and light-blue; state 3: $0.2\% < RE_j \leq 0.3\%$ and blue-green; state 4: $0.3\% < RE_j \leq 0.4\%$ and green; state 5: $0.4\% < RE_j \leq 0.6\%$ and yellow.

Finally, the relative errors RE_A, RE_B, and RE_C are introduced to describe the accuracy of the target ranging as follows:

$$RE_A = \frac{|\Delta d_A|}{d_{T_A}} \times 100\%,$$
$$RE_B = \frac{|\Delta d_B|}{d_{T_B}} \times 100\%,$$
$$RE_C = \frac{|\Delta d_C|}{d_{T_C}} \times 100\%, \quad (35)$$

where the symbol "| |" represents absolute value. We quantize these relative errors for observation. State 1: $0 < RE_A, RE_B, RE_C \leq 0.1\%$; state 2: $0.1\% < RE_A, RE_B, RE_C \leq 0.2\%$; state 3: $0.2\% < RE_A, RE_B, RE_C \leq 0.3\%$; state 4: $0.3\% < RE_A, RE_B, RE_C \leq 0.4\%$; state 5: $0.4\% < RE_A, RE_B, RE_C \leq 0.6\%$. Under high-quality lag chaotic synchronizations, figure 9 depicts the evolutions of these three relative errors in the parameter spaces of τ and τ_A, τ and τ_B, τ and τ_C. It is found from Fig. 9 that their relative errors are all less than 1%, and stay in state 1 in these three large parameter spaces. In addition, when the channel delays τ_A, τ_B, and τ_C are all fixed at 10 ns or 16 ns, their relative errors appear an increase in a slight fluctuation and reach to 0.55%. Therefore, all relative errors of these three targets ranging are small and less than 0.6%, indicating that the ranging scheme can achieve high accuracy.

From these results observed from Figs. 6–8, under high-quality lag chaotic synchronization obtained by the delayed-based reservoir computing approach, the ranging to three targets has good real-time stability. Their absolute errors reach millimeter magnitude, and their relative errors are very small and less than 0.6%.

4. Conclusions

To sum up, we proposed to use a machine-learning technique by means of three parallel optical chaotic reservoirs for realizing the ranging to three targets, respectively. The system proposed consists of the driving three-element laser array with self-feedback, multi-target detection, three input layers, three parallel reservoirs, three output layers, and ranging calculation. Here, these three optical reservoir computers are implemented by the chaotic three-element laser array with both delay-time feedback and optical injection. Three-channel delayed probe signals from the driving three-element laser array with self-feedback are modeled by these three trained reservoir computers, respectively. Our findings show that any one-channel delayed probe signal can synchronize well with its corresponding trained reservoir computer. In other words, high-quality lag chaotic synchronization between them can be achieved even despite the existence of some mismatches between the key parameters of the response three-element laser array and the driving three-element laser array. In addition, the three-channel synchronized probe signals are utilized for the ranging to three targets. Our investigation results indicate that stable and real-time ranging can be achieved for three targets.

Significantly, most previous works focused on laser-based on chaotic radar ranging by using the cross-correlation between the reflected return signal and the replica of the signal transmitted.[1–9,15,16] In these works, the resolution is used to judge the accuracy of the ranging to target. Such correlation-based methods take advantage of the broad bandwidth of the chaotic laser and can achieve resolution up to centimeter-level, indicating that the absolute errors for the ranging to target reach centimeter level. Our previous works reported in Refs. [18,19] explored another new way of implementing the ranging to target by using the synchronized chaotic lidar between driving laser and response one, where the relative errors for the ranging were obtained as less than 2.7% and 11%, respectively, based on the traditional complete chaos theory. By comparison, in this paper, based on the optical reservoir computing approach, the absolute errors for the ranging to multi-target reach millimeter level, and the corresponding relative errors are very small and less than 0.6%. Therefore, the results presented in this paper are better than those in the other reported works. Moreover, when the driving lasers and the response ones consist of four or more-element laser array, four or more-channel delayed probe signals from the driving four or more-element laser array with self-feedback can be modeled by the four or more reservoir computers implemented by the response four or more-element laser array with both delay-time feedback and optical injection, respectively. Using the reservoir computing method, any one of the four or more-channel delayed probe signals can synchronize well with its corresponding trained reservoir computer. Under this condition, the stable and real-time ranging can be realized for four

or more targets.

Acknowledgments

Project supported by the National Natural Science Foundation of China (Grant No. 62075168), GuangDong Basic and Applied Basic Research Foundation (Grant No. 2020A1515011088), and Special Project in Key Fields of Guangdong Provincial Department of Education of China (Grant No. 2020ZDZX3052 and 2019KZDZX1025).

References

[1] Myneni K, Barr T, Reed B, Pethel S and Corron N 2001 *Appl. Phys. Lett.* **78** 1496
[2] Lin F Y and Liu J M 2004 *IEEE J. Sel. Top. Quantum Electron.* **10** 991
[3] Lin F Y and Liu J M 2004 *IEEE J. Sel. Top. Quantum Electron.* **40** 815
[4] Wang B, Wang Y, Lingqin K and Wang A 2008 *Chin. Opt. Lett.* **6** 868
[5] Wang B, Zhao T and Wang H 2012 *Chin. Opt. Lett.* **10** 2801
[6] Zhao Y, Zhang J C, Jia Z W, Liu Y H, Zhuo N, Zhai S Q, Liu F Q and Wang Z G 2016 *Chin. Phys. Lett.* **33** 123201
[7] Du P, Geng D, Wang W and Gong M 2015 *Opt. Eng.* **54** 114102
[8] Wang L, Guo Y, Li P, Zhao T, Wang Y and Wang A 2017 *IEEE Photon. Technol. Lett.* **1** 1
[9] Zhong D, Zeng N, Yang H and Xu Z 2021 *Opt. Exp.* **29** 7809
[10] Bucolo M, Caponetto R, Fortuna L, Frasca M and Rizzo A 2003 *IEEE Circuits Sys. Mag.* **2** 4
[11] Li G 2003 *Microw. Opt. Technol. Lett.* **39** 446
[12] Qiao S, Chen K and Jiang T 2007 *Prog. Electromagn. Res.* **75** 225
[13] Hara Y, Hara T, Seo T, Yanagisawa H, Ratliff P and Machowskg W 2002 *Pro. IEEE Conf.* **1** 227
[14] Subramanian V V and Leung H 2005 *IEEE Signal Process. Lett.* **12** 528
[15] Zhang M, Ji Y, Zhang Y, Wu Y, Xu H and Xu W 2014 *IEEE Photon. J.* **6** 1
[16] Xu H, Wang B, Han H, Liu L, Li J, Wang Y, Wang A and Xu W 2015 *Int. J. Bifurc. Chaos* **25** 1530029
[17] Yao T, Zhu D, Ben D and Pan S 2015 *Opt. Lett.* **40** 1631
[18] Zhong D Z, Xu G, Luo W and Xiao Z 2017 *Opt. Exp.* **25** 21684
[19] Zhong D Z, Xiao Z, Yang G, Zhen N and Yang H 2019 *Opt. Exp.* **27** 9857
[20] Wu W T, Liao Y H and Lin F Y 2010 *Opt. Exp.* **18** 26155
[21] Liu J, Wu Z M and Xia G Q 2009 *Opt. Exp.* **17** 12619
[22] Jiang N, Pan W, Yan L, Luo B, Zhang W, Xiang S, Yang L and Zheng D 2010 *Light. Technol. J.* **28** 1978
[23] Mengue A and Essimbi B 2012 *Nonlinear Dyn.* **70** 1241
[24] Jaeger H and Haas H 2004 *Science* **304** 78
[25] Pathak J, Lu Z, Hunt B, Girvan M and Ott E 2004 *Science* **304** 78
[26] Lu Z, Hunt B and Ott E 2018 *Chaos* **28** 061104
[27] Pathak J, Hunt B, Girvan M, Lu Z and Ott E 2018 *Phys. Rev. Lett.* **120** 024102
[28] Appeltant L, Soriano M, Van der Sande G, Danckaert J, Massar S, Dambre J, Schrauwen B, Mirasso C and Fischer I 2011 *Nat. Commun.* **2** 468
[29] Weng T, Yang H, Gu C, Zhang J and Small M 2019 *Phys. Rev. E* **99** 042203
[30] Larger L, Soriano M, Brunner D, Appeltant L, Pesquera L, Mirasso C and Fischer I 2019 *Opt. Exp.* **20** 3241
[31] Paquot Y, Duport F, Smerieri A, Dambre J, Schrauwen B, Haelterman M and Massar S 2012 *Sci. Rep.* **2** 287
[32] Soriano M C, Ortin S, Brunner D, Larger L, Mirasso C R, Fischer I and Pesquera L 2013 *Opt. Exp.* **21** 12
[33] Duport F, Schneider B, Smerieri A, Haelterman M and Massar S 2012 *Opt. Exp.* **20** 22783
[34] Dejonckheere A, Duport F, Smerieri A, Fang L, Oudar J L, Haelterman M and Massar S 2014 *Opt. Express* **22** 10868
[35] Vinckier Q, Duport F, Smerieri A, Vandoorne K, Bienstman P, Haelterman M and Massar S 2015 *Optica* **2** 438
[36] Brunner D, Soriano M, Mirasso C and Fischer I 2013 *Nat. Commun.* **4** 1364
[37] Kuriki Y, Nakayama J, Takano K and Uchida A 2018 *Opt. Exp.* **26** 5777
[38] Nguimdo R and Erneux T 2019 *Opt. Lett.* **44** 49
[39] Jaeger H 2001 *Ger. Natl. Res. Inst. for Comput. Sci.* **1** 148
[40] Lukosevecius M, Jaeger H and Schrauwen B 2012 *KI-Künstliche Intelligenz* **26** 365
[41] Hou Y, Xia G Q, Yang W, Wang D, Jayaprasath E, Jiang Z, H Chunxia and Wu Z 2018 *Opt. Exp.* **26** 10211
[42] Zhong D, Yang H, Xi J, Zeng N, Xu Z and Fuqin D 2021 *Opt. Exp.* **29** 5279
[43] Amil P, Soriano M and Masoller C 2019 *Chaos* **29** 113111
[44] Bao X, Zhao Q, Yin H and Qin J 2018 *Mod. Phys. Lett. B* **32** 1850150
[45] Triefenbach F, Jalalvand A, Schrauwen B and Martens J P 2010 *Adv. Neural Inf. Process. Syst.* **1** 2307
[46] Boccato L, Lopes A, Attux R and Von Zuben F 2011 *Proc. Int. Jt. Conf. on Neural Networks* pp. 580–587
[47] Antonik P, Gulina M, Pauwels J and Massar S 2018 *Phys. Rev. E* **98** 012215
[48] Zhong D, Yang H, Xi J, Zeng N and Xu Z 2020 *Opt. Exp.* **28** 25778
[49] Hou Y, Yi L, Xia G and Wu Z 2017 *IEEE Photon. J.* **9** 1
[50] Nakayama J, Kanno K and Uchida A 2016 *Opt. Exp.* **24** 8679
[51] Li N, Susanto H, Cemlyn B, Henning I and Adams M 2018 *Sci. Rep.* **8** 109